Title

Investigation of the cesium activation of GaN photocathodes by low-energy electron microscopy

Journal

Physical Review Applied, 22(3)

ISSN

2331-7043

Authors

Sauty, Mylène

Johnson, Cameron W

Tak, Tanay

et al.

Publication Date

2024-09-01

DOI

10.1103/physrevapplied.22.034005

Investigation of the cesium activation of GaN photocathodes by low-energy electron microscopy

Mylène Sauty,[1,*] Cameron W. Johnson,[2] Tanay Tak,[3] Wan Ying Ho,[3] Yi Chao Chow,[3] James S. Speck,[3] Andreas K. Schmid,[2] Claude Weisbuch,[1,3] and Jacques Peretti[1]

[1] *Laboratoire de Physique de la Matière Condensée, Ecole polytechnique, CNRS, Institut Polytechnique de Paris, Palaiseau 91120, France*

[2] *Molecular Foundry, Lawrence Berkeley National Laboratory, Berkeley, California 94720, USA*

[3] *Materials Department, University of California, Santa Barbara, California 93106, USA*

Low-energy electron microscopy (LEEM) was performed on p-GaN samples during *in situ* cesium deposition. LEEM images of electron reflectivity recorded as a function of the incident electron energy at different Cs coverages allowed to spatially resolve the evolution of the local work function (WF) during the activation process. While the average WF drops by more than 3 eV, the local WF remains quite uniform across the surface throughout the activation process. Maximum fluctuations of less than 0.2 eV were observed in the WF maps for Cs coverage of a fraction of a monolayer. These fluctuations are mainly related to the surface topography, in particular, to the atomic steps' structure, which replicates the substrate miscut. Apart from these weak spatial fluctuations, no Cs clusters that would induce strong local WF contrast were observed at the scale of the 20-nm resolution of the measurements. These observations agree with the simple model of semiconductor activation to negative electron affinity that describes the formation of a dipole layer as responsible for the lowering of the WF. Additionally, at complete Cs coverage, the WF becomes fully homogeneous over the surface, smoothing out features originating from defects and topography.

I. INTRODUCTION

The deposition of a monolayer of an alkali metal on the surface of a p-type semiconductor to reduce its work function (WF) and reach effective negative electron affinity (NEA) has been used for decades [1–3] to produce efficient photocathodes operating in the near-infrared and visible range [4,5]. These electron sources, mainly based on GaAs technology, are used in fundamental physics experiments, in particular, to produce spin-polarized electron sources to study spin-dependent phenomena in condensed matter [6,7] or in fundamental interactions [8–10], as well as in light-detection devices, such as photomultiplier tubes and night-vision systems [11,12]. Large band-gap materials, such as GaN, can be easily activated to NEA and turn out to give efficient photocathodes in the visible and near UV range after the deposition of a Cs monolayer [13–18], allowing for the realization of high-performance photomultipliers and solar blind-vision systems [19,20]. Additionally, the situation of NEA of the cesiated semiconductor gives direct access to the low-energy conduction electrons. Exciting the sample by an external source of near band-gap photons enables low-energy photoemission spectroscopy, which gives information on the semiconductor conduction band structure, which has been successfully applied to GaAs, InP, Si, and GaN among others [21–25]. Alternatively, cesiated optoelectronic devices can be studied *in situ* by electroemission spectroscopy and microscopy [26–29].

In the view of improving photoemitters, the cesiation process of GaAs was studied with various microscopy and spectroscopy techniques, most often with a goal of realizing the minimum WF and the best stability over time [30–32]. Low-energy electron microscopy (LEEM) was used to follow the activation of GaAs photocathodes to NEA by measuring the spatially averaged WF during Cs deposition [33]. At the end of the cesiation, the photoemission current, imaged with 20-nm spatial resolution, was observed to be homogeneous over the whole sample surface. In other studies, Cs clusters nucleated on step edges were observed by STM [31], while a phase transition from an insulating to a metallic phase at full surface coverage was characterized by XPS and photoreflectance spectroscopy on GaAs (001) [34–36]. In general, a strong dependence of the cesiated surface properties on the sample preparation, crystalline orientation, and

*Contact author: mylene.sauty@cea.fr

termination was observed. However, none of these studies presented a mapping of the local WF and its evolution during the cesiation process. In nitride materials, although extensive studies were pursued to characterize the performance of photocathodes depending on the sample characteristics, surface preparation, and Cs deposition procedure [14–16,37,38], the microscopic structure and properties of the Cs layer remain poorly understood. For example, GaN photocathodes show large values of thermal emittance, or equivalently, of mean transverse energy (MTE) [4,5], that could *a priori* be linked to the heterogeneity of the Cs layer [39]. Moreover, the homogeneity of the Cs coverage is of primary significance for the interpretation of photoemission and electroemission measurements for example in the recent study of the spatial distribution of electroemitted electrons from cesiated devices [28,29].

In the present work, we use LEEM [6] to study the surface activation of p-doped GaN by cesium deposition. We combine two abilities of LEEM: (i) mapping the local WF of a surface by fitting the drop of the spatially resolved low-energy electron reflectivity when sweeping the incident electron energy [40–42]; (ii) performing *in situ* LEEM while depositing an alkali metal on a surface [33]. Unlike most common approaches where the cesiation process is monitored by measuring the total photoemission current under excitation with near-band-gap light, we can perform a direct mapping of the local surface WF as a function of Cs coverage. We show that, while the average WF drops by more than 3 eV during the whole Cs deposition, the local WF remains quite homogeneous. This indicates that Cs atoms are distributed homogeneously without any evidence of Cs clustering down to the resolution limit of the measurement, of about 10–20 nm. The work-function reduction is well reproduced by the simple Topping model that describes the formation of a dipole layer as a function of Cs coverage [43,44]. At submonolayer coverages, only weak WF heterogeneities of less than 0.2 eV across the surface were observed that correspond to spatial variations of the local Cs density correlated to surface topography structures (atomic steps and defects) leading to differences in adsorption, desorption, and diffusion of the Cs atoms. Then, when the surface activation is completed, which occurs for a Cs coverage of about 1 monolayer, the WF becomes uniform.

II. *IN SITU* CESIUM DEPOSITION IN THE LEEM

The principle of the LEEM is shown in Fig. 1(a). A high-energy electron beam is decelerated near the sample at a tunable low-energy E of a few eV, and with an energy spread of typically 100 meV. Reflected electrons are reaccelerated to their original energy and subsequently travel through the imaging column to the electron camera. Sweeping the incident electron-beam energy allows the measurement of I-V curves (reflected electron current I versus voltage V). Typically, electrons experience a mirror-mode transition when their energy is equal to the WF, leading to the I-V curve shown in Fig. 1(b). The

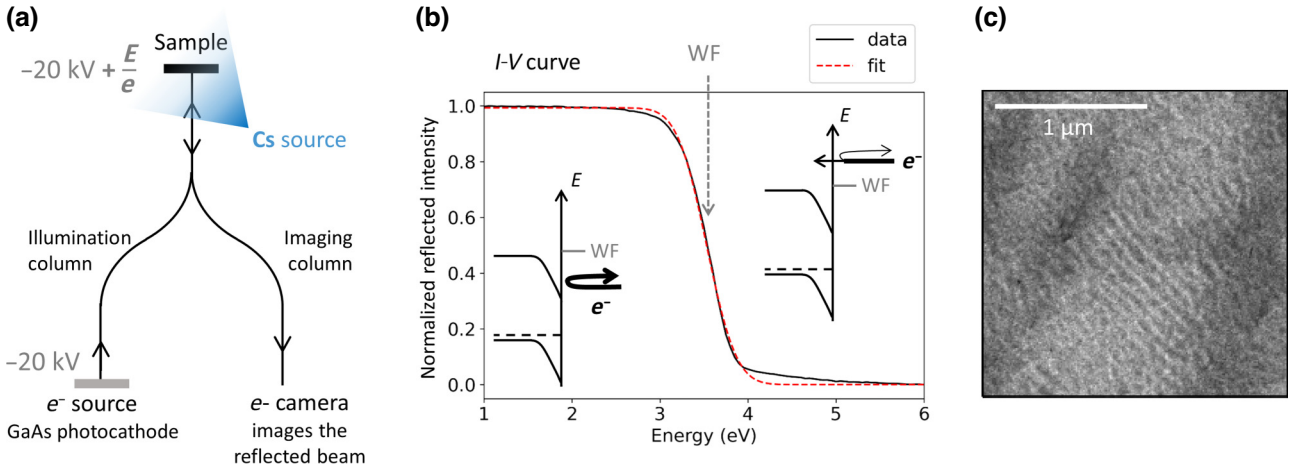

FIG. 1. (a) Schematic of the LEEM experiment: the electron beam produced by a GaAs photocathode is accelerated and transported through the illumination column to the sample. Incident electrons are decelerated just before reaching the sample and electrons reflected at the sample surface are collected back in the imaging column and projected on the electron camera. A Cs dispenser allows activation of the sample surface while performing LEEM measurements. (b) I-V curve: electron current integrated over the full image as a function of the incident electron-beam energy. For energies below the sample WF, all electrons are reflected. For energies above the WF, states are available in the sample for incoming electrons and the reflectivity drops to a value close to 0. A complementary error-function fit (red curve) of the I-V curve allows this mirror-mode transition energy to be captured well, which gives the sample WF. (c) Topography image of a p-GaN sample, obtained when the incident electron energy matches the sample average WF. Contrast arises both from variations of the local WF and from surface roughness, which scatters electrons out of the imaging column. The 100-nm-wide atomic terraces can be seen in the image.

reflected intensity is 1 when the incident energy is far below the WF and decreases when the electrons overcome the sample WF and couple to empty electronic states in the material. Such an I-V curve is reasonably fitted by a complementary error function (red dashed line), that corresponds to a step function broadened by a Gaussian function, which allows recovery of the sample average WF as well as the drop width. The width of the I-V curve's drop is due to different factors, among them local heterogeneities of the WF and charging effects, which will be discussed later. Note that I-V curves can be measured for each pixel of the image, enabling the mapping of the local WF. Additionally, recording the LEEM image at a fixed electron-beam energy, typically around or slightly above the WF, allows imaging of the surface topography. Contrast arises both from the density of states in the sample and from the surface roughness, which scatters electrons out of the imaging path. A LEEM image of a GaN surface is shown in Fig. 1(c), where the atomic terraces appear clearly, here with a spacing of 100 nm, which corresponds to the intentional 0.2° substrate miscut of the sample.

We present results obtained on two p-GaN samples. Additional measurements on one —n-GaN sample are shown for comparison in Appendix A. Note that the same experiments were performed on more than ten samples of various doping, with two different LEEM apparatus. All results were consistent with the measurements presented here. The p-GaN samples were grown by MOCVD on a sapphire substrate, the nucleation layer being followed by 3-μm UID GaN, 2.5-μm n-GaN ([Si] $= 4 \times 10^{18}$cm^{-3}), 1-μm UID GaN and 200-nm p-GaN ([Mg] $= 2.5 \times 10^{19}$cm^{-3}). One of the p-GaN samples was then treated by atomic layer etching (ALE), to remove the top 50 nm, which allows to get rid of the extra Mg dopants that accumulate at the surface during the growth of the p layer [45]. In the remainder of this paper, we will mention these samples as p-GaN and ALE-p-GaN. We first present a fully detailed analysis on the ALE-p-GaN sample. Conclusions are then extended to the p-GaN sample without ALE, which is more standard, and closer to samples used for previous photoemission studies [25,46].

For surface preparation, samples were first chemically treated with an HCl-isopropanol solution, then were introduced into the UHV chamber (base pressure 10×10^{-10} mbar) where they were flash-annealed at about 800°C, 3 times for 1 min. They were finally transferred to the LEEM chamber, where the Cs deposition was performed while imaging the surface and sweeping the electron beam energy to record I-V curve maps during Cs deposition.

III. RESULTS

Figure 2(a) shows the evolution of the I-V curves measured on the ALE-p-GaN sample while depositing Cs on the surface. For each I-V curve, the LEEM reflected current is integrated over a 10-μm field of view (FOV), normalized to its maximum (i.e., its value for an incident electron energy lower than the WF). In the experimental conditions that were used, the whole cesiation process typically took 2.5 h. The I-V curves were recorded every 4 min while continuously depositing Cs, each curve taking about 2 min to be acquired. Curve number is thus equivalent to deposition time. Although the Cs flux was not stopped while recording the curves, it does not affect significantly the WF determination at each deposition time since it is obtained from the drop of the I-V curve, which occurs within only a few seconds. In other words, the continuous cesium deposition does not affect the shape of the I-V

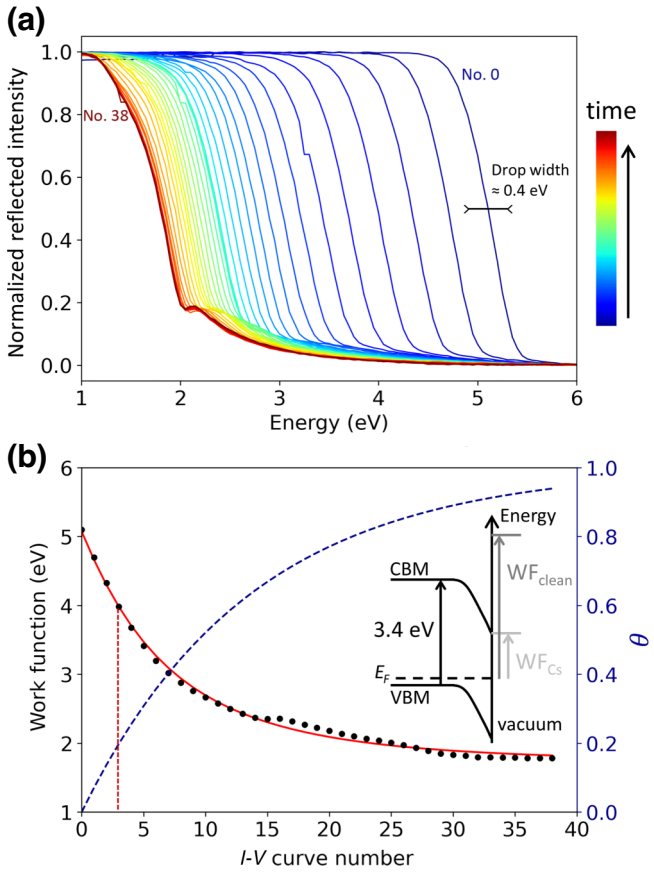

FIG. 2. (a) Evolution of the I-V curve measured on the ALE-p-GaN sample by integrating the LEEM image intensity over the whole 10-μm FOV, during the Cs deposition on the surface. (b) Corresponding WF evolution as a function of time (i.e., I-V curve number) obtained by fitting the reflectivity drop in the I-V curves with a complementary error function. A schematic profile of the conduction and valence band edges in the p-GaN close to the surface is in the inset, along with the position of the vacuum level before and after cesiation. The red line corresponds to a fit to Eqs. (3) and (2), the blue dashed curve indicating the corresponding coverage θ. Curve 3 corresponds to the maximum heterogeneity in the WF maps, obtained for $\theta = 0.2$.

curve drop. The WF evolution with time obtained by fitting the I-V curves drop by a complementary error function is plotted in Fig. 2(b). At the beginning of the measurement, which corresponds to a Cs-free surface, the WF is above 5 eV, consistently with previously reported values on clean p-GaN surfaces [14,15,18]. During Cs deposition, the WF drops by more than 3 eV and reaches a minimum value of 1.8 eV, corresponding to an effective NEA (referred to the conduction-band minimum in the bulk) of about 1.4 eV. Note that, at the end of the cesiation, I-V curves have a characteristic shape, including a bump in reflectivity that appears just above the WF. We believe that this shape results from the electronic structure of the cesiated surface and is left for future discussion [47]. One point to mention is that, at complete Cs coverage (last 5–10 curves), the WF is most probably lower than the value obtained from the error-function fit of the main reflectivity drop of the I-V curve, which instead matches the first available electronic states in the semiconductor band-bending region. Our fitting procedure thus leads to an overestimation of the WF at the end of the cesiation procedure, which however does not significantly affect the analysis of the surface potential mapping presented in this work.

If we consider a simple description where the Cs adsorption rate is proportional to the number of unoccupied sites on the sample surface (i.e., the Cs sticking coefficient is 1 on the free GaN surface and 0 on the Cs-covered surface), the number of Cs-occupied sites n follows a first-order differential equation with time:

$$\frac{dn}{dt} = \frac{1}{t_0}(n_0 - n), \tag{1}$$

where n_0 is the initial density of surface sites and t_0 is a time constant linked to J_{Cs} the incident Cs flux per unit area: $t_0 = (n_0/J_{Cs})$. The solution of this equation is

$$n = n_0(1 - e^{-t/t_0}). \tag{2}$$

As a first approximation, we can consider that the Cs atoms form an assembly of regularly spaced dipoles, once they have transferred their outer electrons to the semiconductor. In his work of 1927, Topping calculated the mutual potential energy induced by such an assembly of dipoles [43]. Divided by the dipole moment of a single Cs atom, it gives the depolarizing field induced by an assembly of Cs atoms. Consequently, the local dipole moment can be calculated from the dipole moment of a single Cs atom and from the depolarizing field due to surrounding Cs atoms. The decrease of the WF from the pristine surface value follows from the potential induced by this local dipole moment [44,48], and the WF evolution is given as

$$\mathrm{WF} = \mathrm{WF}_{\max} - \frac{A\theta}{1 + B\theta^{\frac{3}{2}}}, \tag{3}$$

where $\theta = (n/n_0)$ is the Cs coverage. A and B depend on the site density and on the polarizability and dipole moment of a single Cs atom on the surface [44]. The red curve in Fig. 2(b) corresponds to a fit of the WF evolution to Eq. (3), with θ following Eq. (2). The fitting parameters are $t_0 = 13.6$ (in curve number units), $\mathrm{WF}_{\max} = 5.1$ eV, $A = 5.9$ eV, and $B = 0.77$ [49]. However, only two of the four parameters of the fit are adjustable since the initial and final values of WF are measured ($\mathrm{WF}_{\max} = 5.1$ eV and $\mathrm{WF}_{\min} = 1.8$ eV) and, for $\theta = 1$, we have $\mathrm{WF}_{\max} - \mathrm{WF}_{\min} = A/(1 + B)$. The good agreement of the fit with the experimental data is a signature of a homogeneous distribution of Cs on the surface, ensured by the Coulomb repulsion of positively charged Cs atoms. Slight deviations to the fit at relatively large coverage (around curves 15 to 20, corresponding to $\theta \approx 2/3$) might be due to a more complex behavior of Cs atoms (interaction with the surface or with neighboring Cs atoms, Cs layer reconstruction...) not taken into account in the simple model. More sophisticated models of the coverage-dependent WF curve or *ab initio* calculation such as DFT are developed in the literature to take these abovementioned effects into account [44,50,51]. Deviations to the simple model used here could also be related to changes in the I-V curve shape due to features in the sample density of state in the band-bending region, that would affect our determination of the WF from the error-function fit [47]. Note that, at full coverage, the WF does not start to increase again, contrarily to some curves from the literature [48]. This discrepancy could be due to a different equilibrium between the Cs atoms and the GaN surface, linked to surface cleanliness or to temperature.

The same I-V curve analysis can be performed on each pixel of the LEEM image, fitting each local I-V curve with a complementary error function to extract the local WF. In Figs. 3(a) and 3(c), the obtained WF maps are plotted at different stages of the cesiation, corresponding to curves 0, 2, 9, and 33 in Fig. 2. Figure 3(a) corresponds to a 4 μm × 4 μm area while Fig. 3(c) shows a 1 μm × 1 μm area indicated by a dashed square in the large-scale images. These two sets of maps allow different features to be highlighted appearing at different length scales, as discussed below.

It should first be noted that, Cs clusters of size of the order of or larger than the 10–20 nm spatial resolution of the measurements [52] were not observed at partial Cs surface coverage. They would indeed induce WF spatial variations of about 3 eV, which corresponds to the WF difference between the pristine and the fully covered surface. This does not completely rule out the existence of Cs clusters at smaller scale, as those reported by STM studies on GaAs and Si [31,53,54]. However, we would expect that even small clusters of a few nm should give a strong WF contrast (of a significant fraction of 3 eV, the WF drop from a clean to a fully cesiated surface) at low Cs

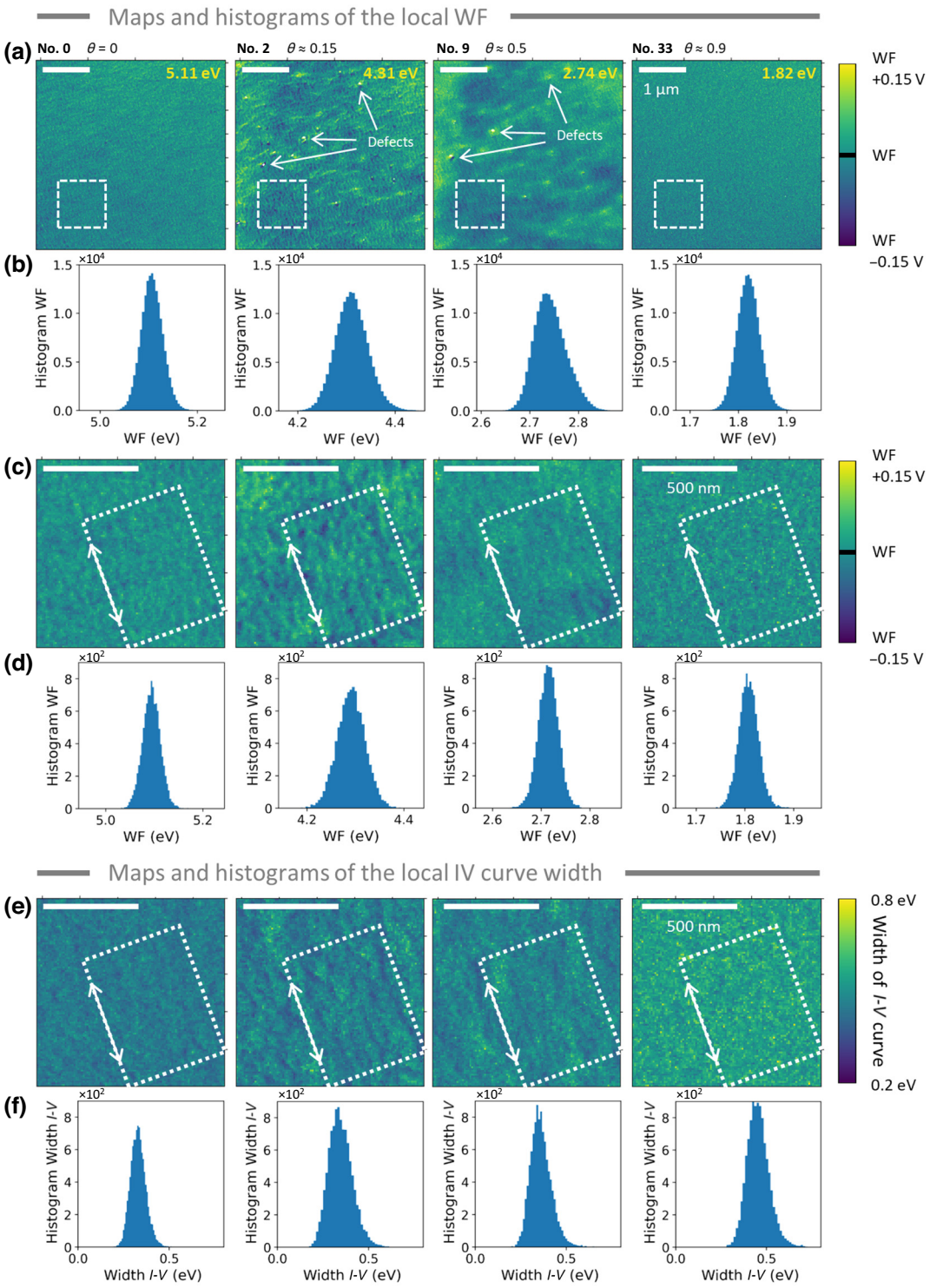

FIG. 3. (a)–(d) Evolution of the spatially resolved WF during the Cs deposition on sample ALE-*p*-GaN. The map numbers correspond to the *I*-*V* curves of Fig. 2. (a) 4-µm FOV. The average WF over the whole FOV is indicated in the top-right corner of the image. Defects and impurities (some of them pointed by a white arrow) are highlighted due to a comparatively higher local WF at partial Cs coverage indicating a lower local Cs density. (b) Histograms of the WF values in the 4-µm FOV maps. (c) 1 µm FOV (indicated by the dashed white square in the 4-µm FOV maps). Stronger contrast at partial coverage arises from a higher Cs density at the step edges, that act as nucleation sites. In both FOV, the last map shows a homogeneous WF at complete Cs coverage, Cs smoothing out defects, and topography. (d) Histograms of the WF values in the 1-µm FOV maps. (e),(f) Evolution of the drop width of the spatially resolved *I*-*V* curves on the 1-µm FOV region. (e) Maps of the local *I*-*V* curves width. Contrast arising from step edges can be observed at partial coverage, with an anticorrelation to the corresponding WF maps, as can be seen in the profiles of Fig. 5. (f) Histograms of the values of the above maps.

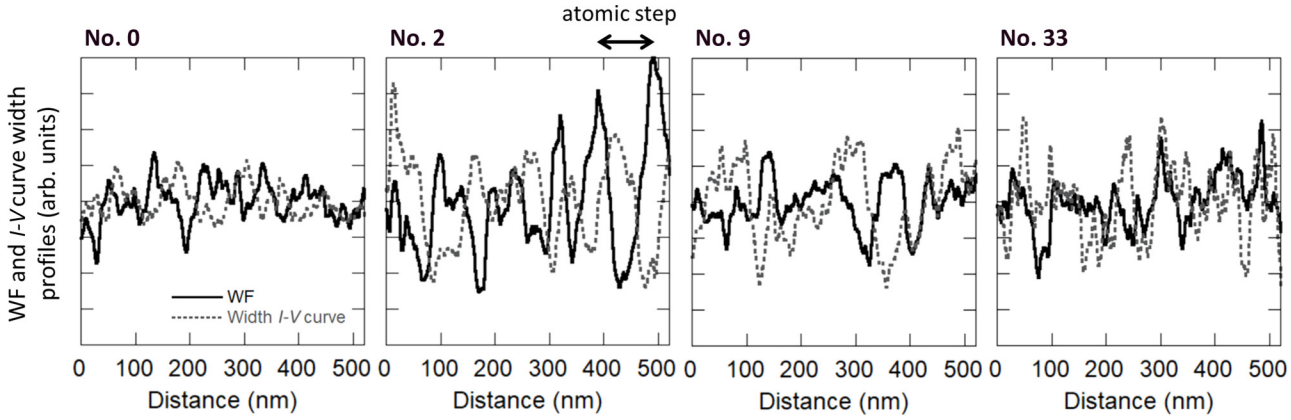

FIG. 4. Spatial amplitude variations of the WF (dark full line) and of the I-V curve width (gray dotted line), inside the white dotted square integrated along the step direction (indicated by a white arrow) in Figs. 3(c) and 3(e), respectively.

densities, when the distance between clusters is larger than the measurement resolution. Instead, the maximum measured variations of WF are less than 0.2 eV, even for Cs coverages of about 10%.

The histograms of the WF values extracted from the WF maps throughout the cesiation process are shown in Figs. 3(b) and 3(d). The change in the width of the histograms shows that the Cs distribution on the GaN surface is not fully homogeneous especially at low Cs coverage. These small WF heterogeneities are mainly correlated with the surface topography and partial Cs coverage highlight steps and defects present on the surface. Structural defects (or impurities, such as residual carbon, the signature of which could be observed in the sample Auger spectrum recorded before the measurement), appear as bright spots (i.e., high WF) right after the cesiation has started, indicating probably a locally lower sticking Cs coefficient. These regions are responsible for the tail at high WF in the histograms of the large FOV WF maps [Fig. 3(b)].

At smaller scale [Fig. 3(c)], contrast arising from atomic steps is visible. This contrast is highlighted in Fig. 4, where the intensity profile inside the white-dotted square of Fig. 3(c), integrated along the step direction, is shown for each map. Note that, in LEEM images, step edges appear dark because of electron scattering out of the specular trajectory of the imaging column. Here in the WF maps, before the Cs deposition starts, a slight dark contrast is also observed at step edges (WF map 0), either due to the electron off-specular scattering or due to a slightly different local work function. After the Cs deposition has started, the contrast of the atomic steps in the WF maps increases, probably due to a preferential occupation of the step edge sites by the Cs atoms, resulting in a locally lower WF. The increase in the topography-related contrast of the WF maps at partial Cs coverage is, as in large FOV WF maps, responsible for the increase in the WF histogram width at moderate Cs coverage [Fig. 3(d)]. The evolution of the standard deviation of the WF histograms in this small FOV region plotted in Fig. 5 versus deposition time (i.e., curve number) and versus average WF shows an abrupt rise right after the start of the Cs deposition and a slow decrease down to a value close to the one of the initial pristine GaN surface. The maximum heterogeneity was observed at a Cs coverage $\theta \approx 0.2$—well before Cs coverage has reached half a monolayer.

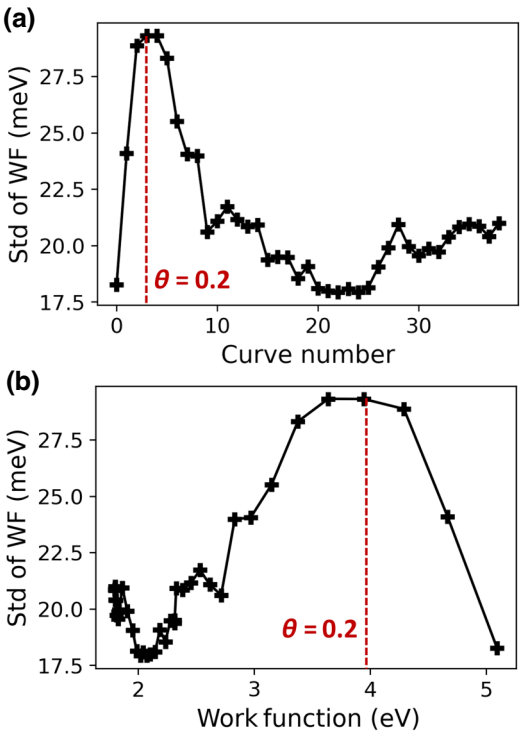

FIG. 5. Standard deviation (std) of the WF values recorded in the small FOV maps of Fig. 3(c), plotted as a function of (a) deposition time (i.e., curve number) and (b) average WF value. The heterogeneity of the Cs layer reaches a maximum for a coverage of about 0.2 before becoming homogeneous again at full coverage.

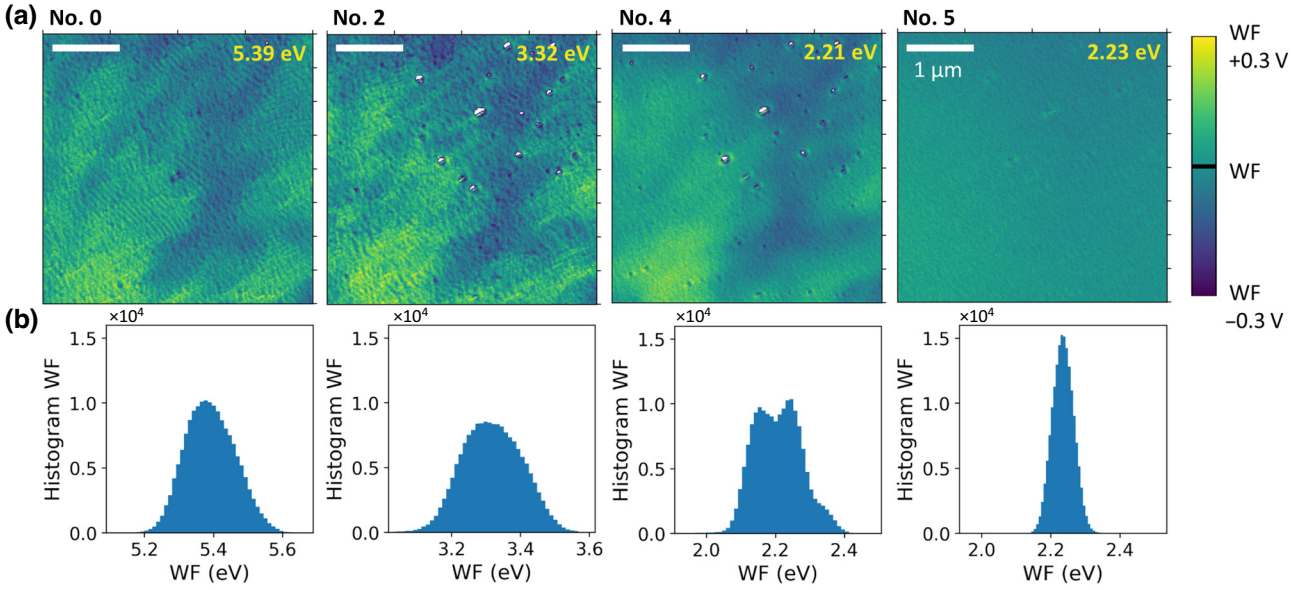

FIG. 6. Cs deposition on sample p-GaN without ALE. (a) Selection of four WF maps before, during, and at the end of the cesiation, with (b) their corresponding histograms. Note the factor of 2 in the color bar and histogram ranges compared to Fig. 3 for sample ALE-p-GaN.

When the Cs monolayer is completed, the WF becomes very homogeneous. As already reported in the case of GaAs [32], this could come from a transition of the conducting character of the Cs layer from insulating to metallic when the percolation threshold between Cs atoms is reached. The signature of such a transition should be a marked change in the surface photovoltage, that can be measured in photoreflectance spectroscopy. However, we could not observe any significant changes of the photoreflectance spectrum as a function of Cs coverage, in experiments performed in similar conditions as in the present LEEM study. Photoreflectance spectra are shown in Appendix B. Alternatively, the diminution of contrast in the WF map between before and after the cesiation could mean that the topographic features before the cesiation arise from local WF difference between step edges and terraces. The Cs layer would then smooth out these WF differences.

In addition to the local WF values and their distribution in energy and space, the width of the I-V curves drops (indicated for sample ALE-p-GaN by a horizontal double arrow in Fig. 2) can be characterized. It is quantified by the same fitting procedure, as the broadening parameter of the complementary error-function fit. On the ALE-p-GaN sample, the width of the I-V curve drop varies from 330 to 440 meV, during the Cs deposition. Note that, these values are much larger than the 100-meV energy spread of the incident electron beam and also than the standard deviation of the WF values in the corresponding WF maps, that are only of a few tens of meV (Fig. 5). Additionally, the fits performed pixel by pixel give very similar widths that on the integrated I-V curves. It means that the broadening of the I-V curve drop is not due to the heterogeneities of the WF across the surface observed in WF maps, unless the characteristic length scale of the WF heterogeneities is smaller than the LEEM resolution, for example, due to a heterogenous Mg dopant distribution in the p-GaN. Apart from WF fluctuations, the broad drop of the I-V curves could be explained by a charging effect due to electron accumulation in the surface downwards band-bending region of p-GaN. This charging effect would happen when electrons have a high enough energy to overcome the WF and enter the sample. Accumulation of electrons trapped in the near-surface band-bending region would induce bands to unbend, shifting the vacuum level upwards, similarly to photovoltage effects after photoexcitation [16]. A slight increase of the electron energy above the WF would allow more electrons to penetrate the sample, leading to an artificial increase of the vacuum level with increasing electron energy, and to a broadening of the I-V curve drop. This explanation is consistent with the observation of much steeper drops on more conductive samples (highly doped p-GaN) and on n-GaN samples having a reversed upwards band-bending favoring electrons to enter the sample (see Appendix A).

The spatially resolved evolution of the width of the I-V curve drop during Cs deposition is plotted in Fig. 3(e) for the same 1 µm × 1 µm FOV region as in Fig. 3(c). The intensity profiles of the maps on the same white-dotted square integrated along the step direction are also plotted

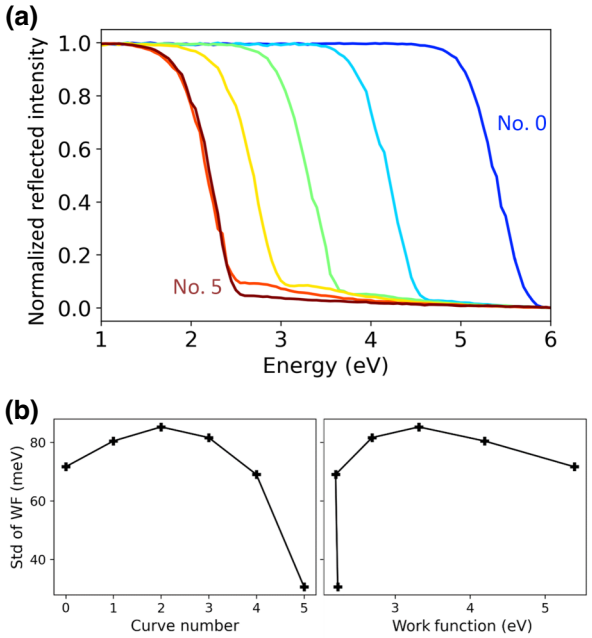

FIG. 7. (a) LEEM average I-V curve on the p-GaN sample during the Cs deposition. (b),(c) Evolution of the standard deviation of the WF values across the maps as a function of time (i.e., curve number) and average WF.

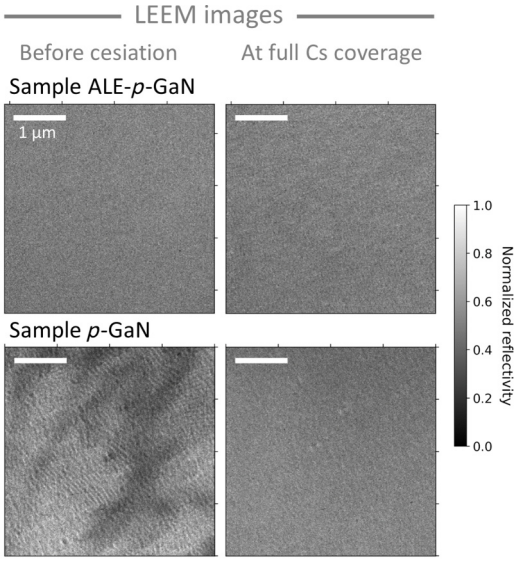

FIG. 8. LEEM images recorded for incident electron energy equal to the WF, for each of the two measured samples, before and after the Cs deposition.

in Fig. 4. A contrast related to the step edges is observed, but is inversed compared to the corresponding WF maps, especially before midcoverage when the WF spread is maximum (map 3). In other words, low WF correlate to large widths, which might be interpreted as an increase of small-scale heterogeneities (= broader I-V curve drop) for increased local Cs coverage (= lower WF). This is a signature of the random distribution of Cs atoms on the surface at a scale smaller than the measurement resolution.

The same *in situ* Cs deposition LEEM measurements were performed on the p-GaN sample without ALE. The evolution of WF maps and histograms across the maps during the Cs deposition as well as the variation of the standard deviation of the WF values across the maps as a function of time and average WF value are shown in Figs. 6 and 7. Figure 8 shows the LEEM images recorded for the incident electron energy equal to the WF, before and at the end of the cesiation. Note that, for both samples, at the end of the cesiation, nearly no more contrast can be observed, indicating a fully homogeneous WF.

The p-GaN sample surface roughness is larger than the ALE-p-GaN one, as can be seen from the stronger contrast in the WF map before cesiation (map 0 in Fig. 6), in the LEEM image before cesiation (Fig. 8), as well as in AFM images recorded on similar p-doped samples with and without ALE, shown in Appendix C. Despite this, during the Cs deposition, a very similar behavior as for the ALE-p-GaN sample was observed, with first an enhancement of the contrast originating from the surface topography and the defects, and finally a smoothing out of the spatial WF fluctuations at full Cs coverage, even more striking on this sample.

IV. CONCLUSION

We have presented a study of the surface activation with Cs of p-type GaN samples by *in situ* LEEM. We have shown that the decrease of the WF during Cs deposition is well accounted for by the Topping model, which describes the formation of a homogeneous dipole layer due to the transfer of the Cs outer-shell electron to the semiconductor. In agreement with this model, the WF maps, obtained from the analysis of the LEEM electron reflectivity images recorded when sweeping the incident electron energy, show that the WF remains spatially homogeneous during the whole Cs deposition process up to the completion of the Cs monolayer. Only a slight increase of the local WF heterogeneity of less than 0.2 eV on 1-µm FOV regions could be observed on the roughest samples, to be compared with the more than 3-eV drop of the average WF during the cesiation. In particular, no Cs clusters could be observed, at least of size larger than the experimental resolution of 10 to 20 nm. As highlighted in the work of Jobst and co-authors [42], would such clusters exist, the measured WF maps would have exhibited much larger variations than actually observed. Other observations, such as the anticorrelation between the WF map and the I-V curve width map, indicate that the Cs atom distribution is homogeneous even at low coverage and at scales smaller than the measurement resolution. The small

WF heterogeneity observed along the cesiation process is shown to be related to the surface morphology, i.e., the roughness (at atomic step level) and the defect density. However, when the Cs monolayer is completed, the surface potential seen by low-energy electrons appears to be smoothed out. This indicates that the large thermal emittance observed in GaN photocathodes is not dominated by heterogeneities in the Cs coverage. Indeed, it is expected that small spatial WF variations as the ones we report should induce mean transverse energies of less than 10 meV [39], more than 10 times lower than values reported in the literature [4,5]. In addition, the spatially homogeneous WF at the end of the cesiation validates the measurements done when studying electronic processes in cesiated nitride compounds and devices with low-energy photoemission and electroemission spectroscopy and microscopy techniques [25–29,46].

ACKNOWLEDGMENTS

We thank Jean-Philippe Banon for fruitful discussions. This work was supported by the French National Research Agency (ANR, TECCLON Grant No. ANR-20-CE05-0037-01) and by the Simons Foundation (Grants No. 1027114 C.W. and No. 601952 J.S.S.). Work at the Molecular Foundry was supported by the Office of Science, Office of Basic Energy Sciences, of the U.S. Department of Energy under Contract No. DE-AC02-05CH11231. Support at UCSB was provided by the Solid State Lighting and Energy Electronics Center (SSLEEC); U.S. Department of Energy under the Office of Energy Efficiency & Renewable Energy (EERE) Award No. DEEE0009691; the University of California, Santa Barbara (UCSB) – Collaborative Research of Engineering, Science and Technology (CREST) program; the National Science Foundation (NSF) RAISE program (Grant No. DMS1839077).

APPENDIX A: CESIATION OF *n*-GaN

The *n*-GaN sample is an Enkris Semiconductor template grown on Sapphire, followed by 3-μm UID GaN and 2-μm *n*-GaN ($[Si] = 4 \times 10^{18} cm^{-3}$).

The same *in situ* Cs deposition LEEM measurements were performed on this sample (Figs. 9 and 10). The evolution of WF maps and histograms across the maps during the Cs deposition as well as the variation of the standard deviation of the WF values across the maps as a function of time and average WF value are shown in Fig. 9. Figure 10(c) shows the LEEM images recorded for the incident electron energy equal to the WF, before and at the end of the cesiation.

The Cs deposition on *n*-GaN follows the same trend as in *p*-GaN, with an enhancement of topography and defect-related features in the WF during the cesiation, but of much smaller amplitude, making it difficult to distinguish from the noise. This is probably related to the weaker LEEM contrast on *n*-GaN, linked to a smoother surface potential and a lower defect density compared to *p*-GaN (induced by Mg clusters in *p*-doped samples, for example). At the

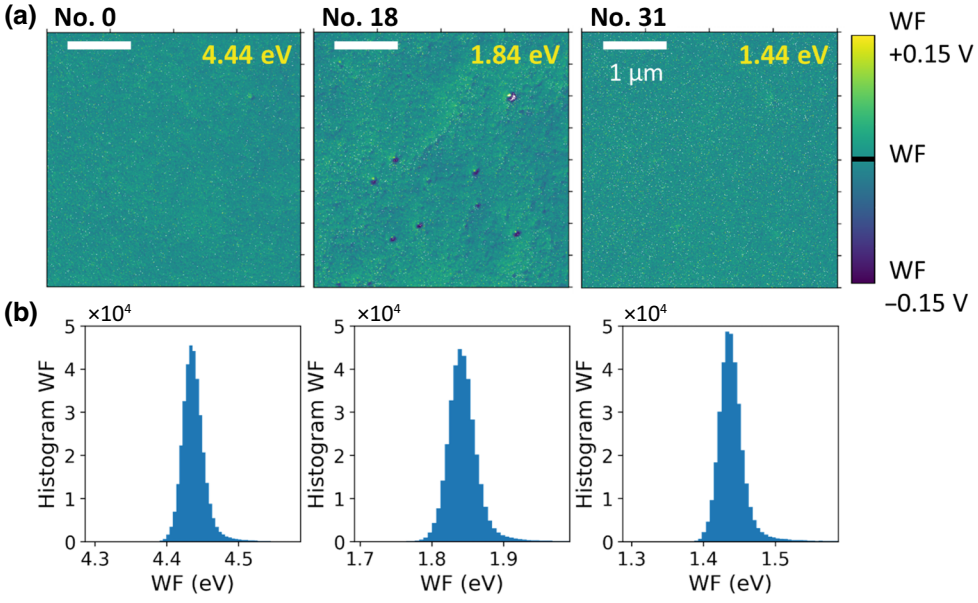

FIG. 9. (a) Selection of three WF maps before, during, and after cesiation of the *n*-GaN sample with (b) their corresponding WF histograms. Note that the color bar and histogram ranges are the same as for sample ALE-*p*-GaN in the main paper.

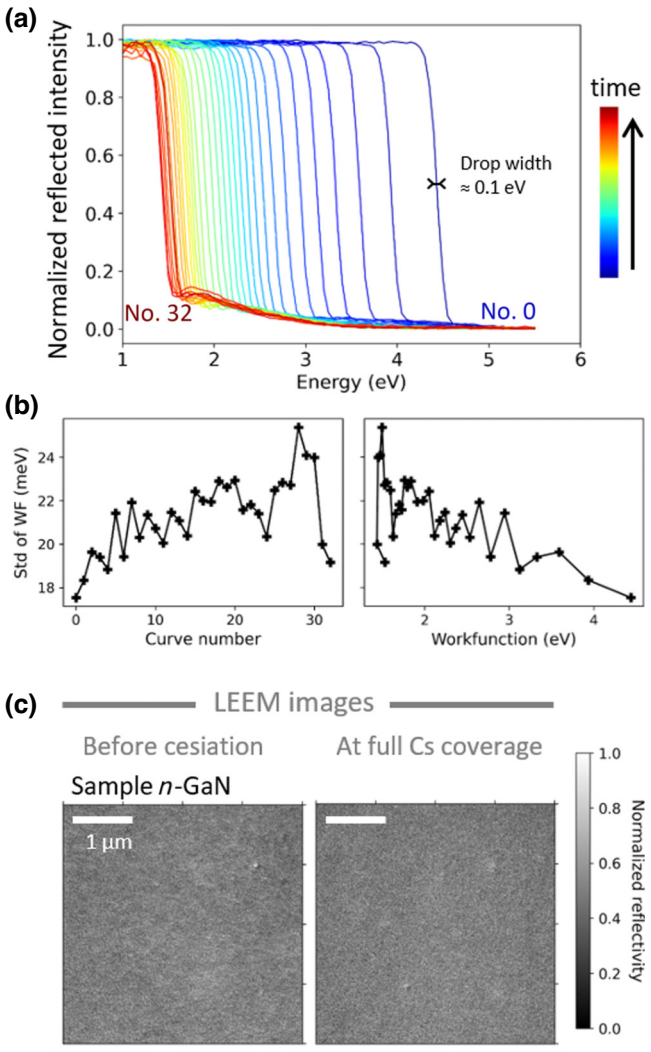

FIG. 10. (a) LEEM average I-V curves recorded during Cs deposition on the n-GaN sample. (b) Evolution of the standard deviation of the WF across the WF maps as a function of time (i.e., curve number) and average WF. (c) LEEM images recorded for incident electron energy equal to the WF, before and after the Cs deposition.

end of the cesiation, the WF also becomes fully homogeneous at the surface. Note that this transition to a smooth WF happens at the very end of the cesiation (here, at the last curve before stopping the Cs flux). Another striking difference with p-GaN is the width of the I-V curve drop [indicated by the horizontal double arrow in Fig. 9(a)]. In the n-GaN sample, the drop is much steeper than in both p-GaN samples, with a broadening parameter of about 100 meV, that corresponds to the energy resolution of the measurement, linked to the energy spread of the electron beam. This is in agreement with the proposed explanations for the broader widths in p-GaN, that are specific to the downwards band-bending region induced by the p doping.

APPENDIX B: PHOTOREFLECTANCE MEASUREMENTS ON p-GaN, BEFORE AND AFTER Cs DEPOSITION

As observed in the WF maps' evolution during Cs deposition on p-GaN, the sample WF becomes very homogeneous at the end of the cesiation, smoothing out any topography or defect-related features. It could be due to a insulator to metal transition of the Cs layer happening near complete coverage. If so, it should induce a strong reduction of photovoltage effects at the sample surface when the Cs layer becomes metallic, that can be probed by photoreflectance measurements.

The photoreflectance of p-GaN before and after Cs deposition was performed on a similar sample to the p-GaN sample (without ALE), under similar conditions than the LEEM study presented in the main text. The sample reflectance was obtained using a photodiode and a UV-enhanced lamp coupled to a monochromator, with an output power of a few µW, at an incidence of 45°. In addition, the sample was illuminated along normal incidence by a continuous-wave laser at 3.54 eV (350 nm), above the band gap of GaN, chopped at a frequency

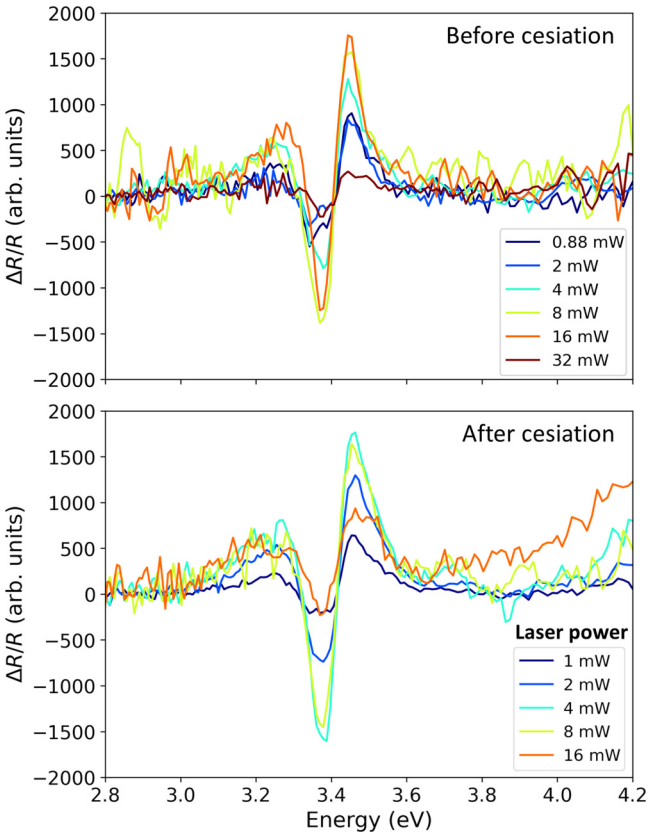

FIG. 11. Photoreflectance spectra recorded on p-GaN, depending on the incident power of the continuous wave laser at 3.54 eV, chopped at 86 Hz. Spectra before and after the Cs deposition do not show significant changes in photovoltage effects.

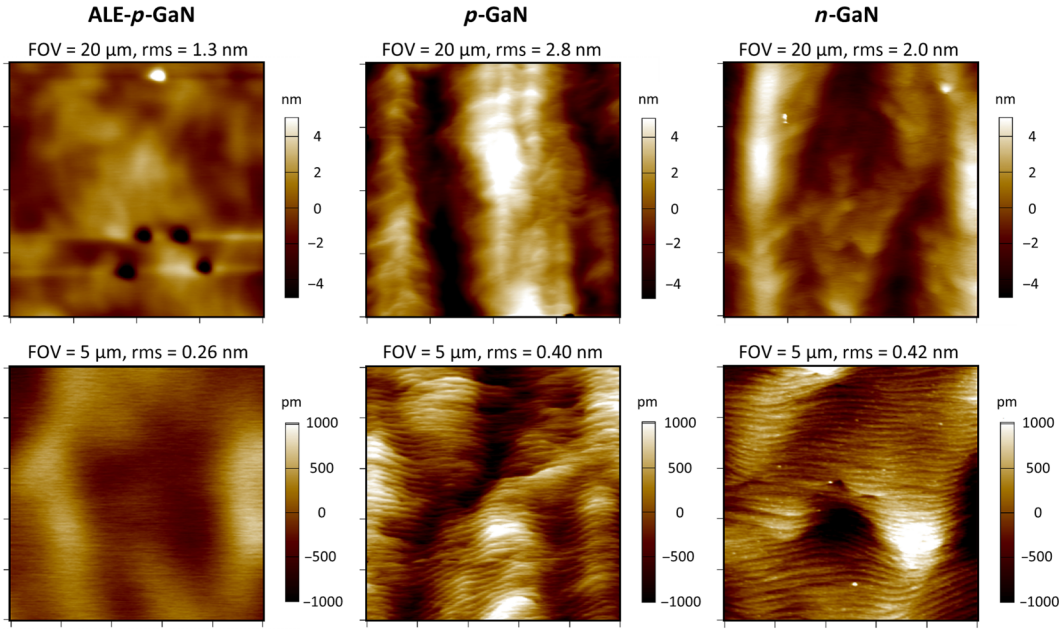

FIG. 12. AFM maps of equivalent ALE-*p*-GaN, *p*-GaN, and *n*-GaN samples, for two different FOV on each. The height standard deviation is indicated as rms for each of the images.

of 86 Hz. The photodiode measuring the reflection of the lamp by the sample was demodulated with a lock-in amplifier, and normalized to the steady-state reflectance. Resulting photoreflectance spectra are shown on Fig. 11, measured before and after Cs deposition, for different laser-incident power, from 1 to 32 mW. Note the nonmonotonic behavior of the photoreflectance amplitude with incident power, maybe due to a photoconductivity effect at high power. However, no significant change in the photoreflectance amplitude can be noticed from these spectra. It does not confirm any transition of the Cs layer conductive character from insulating to metallic. Since the measurement was performed in similar but not identical conditions (different sample, different vacuum chamber, slightly different cleaning procedures) as our LEEM study, we cannot exclude a different behavior of the Cs layer.

APPENDIX C: AFM MAPS

AFM maps recorded on similar samples as the ones studied in the present paper are shown on Fig. 12 for two different fields of view. The corresponding height standard deviation is indicated. Consistently with the LEEM measurement, ALE-*p*-GaN is smoother than *p*-GaN.

[1] J. Scheer and J. van Laar, GaAs-Cs: A new type of photoemitter, Solid State Commun. **3**, 189 (1965).

[2] W. E. Spicer, Photoemissive, photoconductive, and optical absorption studies of alkali-antimony compounds, Phys. Rev. **112**, 114 (1958).

[3] W. E. Spicer, Negative affinity 3–5 photocathodes: Their physics and technology, Appl. Phys. **12**, 115 (1977).

[4] D. Dowell, I. Bazarov, B. Dunham, K. Harkay, C. Hernandez-Garcia, R. Legg, H. Padmore, T. Rao, J. Smedley, and W. Wan, Cathode R & D for future light sources, Nucl. Instrum. Methods Phys. Res., Sect. A **622**, 685 (2010).

[5] J. Schaber, R. Xiang, and N. Gaponik, Review of photocathodes for electron beam sources in particle accelerators, J. Mater. Chem. C **11**, 3162 (2023).

[6] E. Bauer, Low energy electron microscopy, Rep. Prog. Phys. **57**, 895 (1994).

[7] T. Duden and E. Bauer, A compact electron-spin-polarization manipulator, Rev. Sci. Instrum. **66**, 2861 (1995).

[8] D.-A. Luh, Recent polarized photocathode R & D at SLAC, AIP Conf. Proc. **675**, 1029 (2003).

[9] J. Clendenin, A. Brachmann, E. Garwin, S. Harvey, J. Jiang, R. Kirby, D.-A. Luh, T. Maruyama, R. Prepost, C. Prescott, and J. Turner, Recent progress at SLAC extracting high charge from highly polarized photocathodes for future-collider applications, Nucl. Instrum. Methods Phys. Res., Sect. A **536**, 308 (2005).

[10] J. Grames and M. Poelker, *Particle Acceleration and Detection* (Springer International Publishing, 2022), p.261, https://link.springer.com/chapter/10.1007/978-3-031-16715-7_11.

[11] M. Niigaki, T. Nagai, M. Ota, T. Nihashi, and K. Oba, MOCVD growth of GaAs, AlGaAs and its application to transmission photocathodes, Appl. Surf. Sci. **33–34**, 1160 (1988).

[12] K. Chrzanowski, Review of night vision technology, Opto-Electron. Rev. **21**, 153 (2013).

[13] F. Machuca, Y. Sun, Z. Liu, K. Ioakeimidi, P. Pianetta, and R. F. W. Pease, Prospect for high brightness III–nitride electron emitter, J. Vac. Sci. Technol., B **18**, 3042 (2000).

[14] A. A. Pakhnevich, V. V. Bakin, G. E. Shaĭbler, and A. S. Terekhov, Emission of ballistic photoelectrons from p-GaN(Cs,O) with the effective negative electron affinity, Phys. Solid State **49**, 2070 (2007).

[15] A. A. Pakhnevich, V. V. Bakin, A. V. Yaz'kov, G. E. Shaibler, S. V. Shevelev, O. E. Tereshchenko, A. S. Yaroshevich, and A. S. Terekhov, Energy distributions of photoelectrons emitted from p-GaN(Cs, O) with effective negative electron affinity, JETP Lett. **79**, 479 (2004).

[16] S. A. Rozhkov, V. V. Bakin, D. V. Gorshkov, S. N. Kosolobov, and H. E. Scheibler, Surface photovoltage in a p-GaN(Cs) photocathode, J. Phys. Conf. Series **1199**, 012031 (2019).

[17] T. Nishitani, T. Maekawa, M. Tabuchi, T. Meguro, Y. Honda, and H. Amano, Photocathode electron beam sources using GaN and InGaN with NEA surface, Proc. SPIE **9363**, 93630T (2015).

[18] T. Nishitani, M. Tabuchi, H. Amano, T. Maekawa, M. Kuwahara, and T. Meguro, Photoemission lifetime of a negative electron affinity gallium nitride photocathode, J. Vac. Sci. Technol., A **32**, 06F901 (2014).

[19] S. Uchiyama, Y. Takagi, M. Niigaki, H. Kan, and H. Kondoh, GaN-based photocathodes with extremely high quantum efficiency, Appl. Phys. Lett. **86**, 103511 (2005).

[20] Y. Ishigami, K. Akiyama, T. Nagata, K. Kato, T. Ihara, K. Nakamura, I. Mizuno, T. Matsuo, E. Chino, and H. Kyushima, Development of a high-sensitivity UV photocathode using GaN film that works in transmission mode, Proc. SPIE **8359**, 83590U (2012).

[21] H.-J. Drouhin, C. Hermann, and G. Lampel, Photoemission from activated gallium arsenide. I. Very-high-resolution energy distribution curves, Phys. Rev. B **31**, 3859 (1985).

[22] Y. Lassailly, P. Chiaradia, C. Hermann, and G. Lampel, Experimental photoemission results on the low-energy conduction bands of silicon, Phys. Rev. B **41**, 1266 (1990).

[23] J. Peretti, H.-J. Drouhin, D. Paget, and A. Mircéa, Band structure of indium phosphide from near-band-gap photoemission, Phys. Rev. B **44**, 7999 (1991).

[24] J. Peretti, H.-J. Drouhin, and D. Paget, High-resolution energy analysis of field-assisted photoemission: A spectroscopic image of hot-electron transport in semiconductors, Phys. Rev. B **47**, 3603 (1993).

[25] M. Piccardo, L. Martinelli, J. Iveland, N. Young, S. P. DenBaars, S. Nakamura, J. S. Speck, C. Weisbuch, and J. Peretti, Determination of the first satellite valley energy in the conduction band of wurtzite GaN by near-band-gap photoemission spectroscopy, Phys. Rev. B **89**, 235124 (2014).

[26] J. Iveland, L. Martinelli, J. Peretti, J. S. Speck, and C. Weisbuch, Direct measurement of Auger electrons emitted from a semiconductor light-emitting diode under electrical injection: Identification of the dominant mechanism for efficiency droop, Phys. Rev. Lett. **110**, 177406 (2013).

[27] W. Y. Ho, Y. C. Chow, D. J. Myers, F. Wu, J. Peretti, C. Weisbuch, and J. S. Speck, Quantitative correlation of hot electron emission to Auger recombination in the active region of c-plane blue III-N LEDs, Appl. Phys. Lett. **119**, 051105 (2021).

[28] W. Y. Ho, C. W. Johnson, T. Tak, M. Sauty, Y. C. Chow, S. Nakamura, A. Schmid, J. Peretti, C. Weisbuch, and J. S. Speck, Steady-state junction current distribution in p-n GaN diodes measured using low-energy electron microscopy (LEEM), Appl. Phys. Lett. **123**, 031101 (2023).

[29] T. Tak, C. W. Johnson, W. Y. Ho, F. Wu, M. Sauty, S. Rebollo, A. K. Schmid, J. Peretti, Y.-R. Wu, C. Weisbuch, and J. S. Speck, Injection mechanisms in a III-nitride light-emitting diode as seen by self-emissive electron microscopy, Phys. Rev. Appl. **20**, 064045 (2023).

[30] R. Fukuzoe, M. Hirao, D. Yamanaka, Y. Iwabuchi, H. Iijima, and T. Meguro, Preparation of Ga-terminated negative electron affinity-GaAs (100) surface by HCl-isopropanol treatment for nanoanalysis by scanning tunneling microscopy, J. Vac. Sci. Technol., B **36**, 06JK01 (2018).

[31] M. Hirao, D. Yamanaka, T. Yazaki, J. Osako, H. Iijima, T. Shiokawa, H. Akimoto, and T. Meguro, STM study on adsorption structures of Cs on the As-terminated GaAs(001) (2 × 4) surface by alternating supply of Cs and O_2, IEICE Trans. Electron. **E99.C**, 376 (2016).

[32] B. Kierren and D. Paget, Formation of the Cs/GaAs(001) interface: Work function, cesium sticking coefficient, and surface optical anisotropy, J. Vac. Sci. Technol., A **15**, 2074 (1997).

[33] X. Jin, A. A. C. Cotta, G. Chen, A. T. N'Diaye, A. K. Schmid, and N. Yamamoto, Low energy electron microscopy and Auger electron spectroscopy studies of Cs-O activation layer on p-type GaAs photocathode, J. Appl. Phys. **116**, 174509 (2014).

[34] P. Chiaradia, D. Paget, O. Tereshchenko, J. Bonnet, A. Taleb-Ibrahimi, R. Belkhou, and F. Wiame, Insulator–metal phase transitions of alkali atoms on GaAs(001), Surf. Sci. **600**, 287 (2006).

[35] D. Paget, Optical investigation of submonolayer phase transitions of Cs on GaAs(001), Phys. Status Solidi A **170**, 391 (1998).

[36] O. E. Tereshchenko, D. V. Daineka, and D. Paget, Metallicity and disorder at the alkali-metal/GaAs(001) interface, Phys. Rev. B **64**, 085310 (2001).

[37] X. Wang, M. Wang, Y. Liao, L. Yang, Q. Ban, X. Zhang, Z. Wang, and S. Zhang, Negative electron affinity of the GaN photocathode: A review on the basic theory, structure design, fabrication, and performance characterization, J. Mat. Chem. C **9**, 13013 (2021).

[38] M. Kashima, Y. Itokawa, T. Kanai, D. Sato, A. Koizumi, H. Iijima, T. Nishitani, Y. Honda, H. Amano, and T. Meguro, The photoemission characteristics of a NEA InGaN photocathode by simultaneously supplying Cs and O_2, Appl. Surf. Sci. **599**, 153882 (2022).

[39] S. Karkare and I. Bazarov, Effects of surface nonuniformities on the mean transverse energy from photocathodes, Phys. Rev. Appl. **4**, 024015 (2015).

[40] J. Jobst, J. Kautz, M. Mytiliniou, R. M. Tromp, and S. J. van der Molen, Low-energy electron potentiometry, Ultramicroscopy **181**, 74 (2017).

[41] A. L. Cauduro, R. dos Reis, G. Chen, A. K. Schmid, H.-G. Rubahn, and M. Madsen, Work function mapping

of MoO_x thin-films for application in electronic devices, Ultramicroscopy **183**, 99 (2017).
[42] J. Jobst, L. M. Boers, C. Yin, J. Aarts, R. M. Tromp, and S. J. van der Molen, Quantifying work function differences using low-energy electron microscopy: The case of mixed-terminated strontium titanate, Ultramicroscopy **200**, 43 (2019).
[43] J. Topping, On the mutual potential energy of a plane network of doublets, Proc. R. Soc. London, Ser. A 114, 67 (1927).
[44] R. Weber and W. Peria, Work function and structural studies of alkali-covered semiconductors, Surf. Sci. **14**, 13 (1969).
[45] W. Y. Ho, Y. C. Chow, Z. Biegler, K. S. Qwah, T. Tak, A. Wissel-Garcia, I. Liu, F. Wu, S. Nakamura, and J. S. Speck, Atomic layer etching (ALE) of III-nitrides, Appl. Phys. Lett. **123**, 062102 (2023).
[46] M. Sauty, N. M. Lopes, J.-P. Banon, Y. Lassailly, L. Martinelli, A. Alhassan, Y. C. Chow, S. Nakamura, J. S. Speck, C. Weisbuch, and J. Peretti, Localization effect in photoelectron transport induced by alloy disorder in nitride semiconductor compounds, Phys. Rev. Lett. **129**, 216602 (2022).
[47] M. Sauty and J.-P. Banon, (unpublished).
[48] T. U. Kampen, M. Eyckeler, and W. Mönch, Electronic properties of cesium-covered GaN(0001) surfaces, Appl. Surf. Sci. **123–124**, 28 (1998).
[49] Note that we find a reasonable fitting for t_0 within a range of ± 5, which impacts the precision in the determination of the Cs coverage depending on time.
[50] H. Clemens, J. Von Wienskowski, and W. Mönch, On the interaction of cesium with cleaved GaAs(110) and Ge(111) surfaces: Work function measurements and adsorption site model, Surf. Sci. **78**, 648 (1978).
[51] M. Yang, B. Chang, and M. Wang, Cesium, oxygen coadsorption on AlGaN(0001) surface: Experimental research and ab initio calculations, J. Mater. Sci. - Mater. Electron. **26**, 2181 (2015).
[52] The spatial resolution of the LEEM was calibrated to be 8 nm in the best operating conditions. In the conditions of these measurements, mainly due to a nonoptimal distance between the sample and the first high-voltage lens chosen to prevent arcing when cesiating the sample, we estimated the resolution to be slightly worsened, of about 10 to 20 nm. This resolution was estimated using lithographically defined features on different samples measured with similar operating conditions.
[53] L. J. Whitman, J. A. Stroscio, R. A. Dragoset, and R. J. Celotta, Geometric and electronic properties of Cs structures on III-V (110) surfaces: From 1D and 2D insulators to 3D metals, Phys. Rev. Lett. **66**, 1338 (1991).
[54] K. Wu, Y. Fujikawa, Y. Takamura, and T. Sakurai, Alkali metal adsorption on the Si(111)-(7 × 7) surface, Chin. J. Phys. **43**, 197 (2005).